Tuning CH4 Productivity from Visible Light-Driven Gas-Phase CO2 Photocatalytic Reduction on Doped g-C3N4/TiO2 Heterojunctions

Leila Hammoud, Clément Marchal, Christophe Colbeau-Justin, Joumana Toufaily, Tayssir Hamieh, Valérie Caps, Valérie Keller

Energy Technology
Generation, Conversion, Storage, Distribution
www.entechnol.de

Tuning CH_4 Productivity from Visible Light-Driven Gas-Phase CO_2 Photocatalytic Reduction on Doped g-C_3N_4/TiO_2 Heterojunctions

*Leila Hammoud, Clément Marchal, Christophe Colbeau-Justin, Joumana Toufaily, Tayssir Hamieh, Valérie Caps, and Valérie Keller**

Herein, visible light-driven gas-phase photocatalytic CO_2 reduction into CH_4 is tuned by designing optimized three-component Au/doped C_3N_4/TiO_2 composite photocatalysts. The key point strategy consists in the formation of high-quality C_3N_4/TiO_2 heterojunction by associating low containing doped graphitic carbon nitride to commercially available TiO_2 UV-100. Those heterojunctions result in both visible light sensitization and increased charge-carrier separation. Further deposition of small Au nanoparticles (≈3 nm), quite exclusively onto TiO_2 surfaces, mainly acts as electron trapping/cocatalytic functions without excluding surface plasmonic effects. The resulting doped g-C_3N_4 material exhibits enhanced visible light harvesting properties, especially in the case of C-doping. In addition, it is assumed that B– and C–C_3N_4 doping, leading to a more or less lower conduction band position, is the impacting factor toward total CH_4 selectivity achievement. The (0.77 wt%)Au/(0.59 wt%)C–C_3N_4/TiO_2 composite photocatalyst, exhibiting the best compromise between the various impacting factors, leads to a continuous productivity rate of CH_4 of 8.5 μmol h^{-1} g^{-1} under visible light irradiation over at least 10 h. To the best of knowledge, this level of performance is unprecedented under continuous gas-phase flowing CO_2 in the presence of water as reducing agent, without addition of any sacrificial agent.

1. Introduction

In the frame of CO_2 transformation into clean fuels which could be an interesting alternative both to global warming limitation and depletion of fossil fuels, CO_2 photocatalytic reduction is considered as being a promising technology for converting CO_2 into light-driven alcohols and hydrocarbons, as reported in several reviews summing up the state-of-the-art on that topic.[1–3] Indeed, this green alternative has received great and increased attention since the work dealing with photoelectrocatalytic reduction of CO_2 by Inoue et al.[4] However, CO_2 is one of the most stable molecules. Inspired by the natural photosynthesis process in which reduction of CO_2 occurs with H_2O using solar irradiation, water is considered as being the most suitable hydrogen donor (mainly implied as H^+ donor in CO_2 reduction mechanism) for CO_2 artificial photocatalytic reduction. Its main drawback is that it easily recombines into H_2, consuming photogenerated electrons thus lowering carbon-based valuable compounds yields formation.[5] Indeed, considering that the redox potential for CO_2 reduction is close to that for H_2O reduction to H_2 (however slightly more favorable), that the activation of H_2O is easier than that of CO_2, and that the formation of CH_4 needs eight electrons (instead of two for H_2 production), the reduction of CO_2 is kinetically less favored. Consequently, different strategies can be carried out in order to drive selective production of CH_4, compared to H_2, such as suitable cocatalyst deposition,[6] use of plasmonic metal-based nanostructures, use of semiconductors able to generate electrons with appropriate reduction potential, working with

L. Hammoud, C. Marchal, V. Caps, V. Keller
ICPEES
Institut de Chimie et des Procédés pour l'Energie, l'Environnement et la Santé
CNRS/Université de Strasbourg
UMR 7515 (CNRS)
25 rue Becquerel, 67087 Strasbourg, Cedex, France
E-mail: vkeller@unistra.fr

The ORCID identification number(s) for the author(s) of this article can be found under https://doi.org/10.1002/ente.202201363.

DOI: 10.1002/ente.202201363

C. Colbeau-Justin
ICP
Institut de Chimie Physique, CNRS UMR 8000
Université Paris-Saclay
Bâtiment 349, 91405 Orsay Cedex, France

J. Toufaily, T. Hamieh
MCEMA, Laboratory of Materials, Catalysis, Environment and Analytical Methods
Lebanese University Hadath
Campus Rafic Hariri, Bayrouth, Lebanon

T. Hamieh
Faculty of Science and Engineering
Universiteit Maastricht
P.O. Box 616, 6200 ED Maastricht, The Netherlands

continuous CO_2 gas-phase flow with increased contact time to allow pathways involving several electron and H^+ transfers, using high surface area materials increasing CO_2 adsorption and bandgap engineering for visible light harvesting, as well as heterojunction formation for enhanced charge-carrier separation.[7–9] Since a few years a large and increased number of semiconductors and some metal sulfides have been reported for photocatalytic CO_2 reduction with water. However, the photocatalytic activity, stability, and product selectivity are far away from interesting consideration. Among a large variety of semiconductors investigated for photocatalytic CO_2 reduction, it was concluded that TiO_2-based photocatalysts exhibit the best activity, taking into consideration chemical stability, and mainly moderate cost.[10] TiO_2-heterojunction photocatalysts appear as a promising strategy. Numerous studies are dealing with TiO_2-SC_2 heterojunctions. Several of them relating the successful formation the TiO_2/g-C_3N_4 show that the photoactivity for environmental or solar fuels applications can be successfully promoted, thanks to enhanced visible light absorption and charge-carrier separation.[11–14] In the last years, g-C_3N_4 has been shown as being an effective semiconductor to facilitate photocatalytic CO_2 reduction because of its high conduction band energy, thus enabling the CO_2 reduction half-reaction.[15] However, it has been observed that the selectivity toward a desired reduction product is affected by the nanostructure design and the choice of the associated photoactive component in the g-C_3N_4-based nanocomposites.[16,17] Despite its visible light sensitization effect, and appropriate positions of CB and VB in respect to H_2O oxidation and CO_2 reduction into CH_4, g-C_3N_4 suffers from poor utilization of the photoexcited charge carriers and often from low CO_2 adsorption, resulting mainly from deficiency of electron donation sites and unappropriate electronic structure.[18] Furthermore, low efficient interlayer charge transfer also results in increased recombination rate.[19,20] To overcome some of these limitations and improve the photocatalytic performance, several protocols are proposed, such as nanostructuring,[21] doping by metals and nonmetals,[12,22] exfoliation,[23] controllable morphologies with different geometric shapes,[24] and copolymerization.[25] Doping of graphitic carbon nitride with nonmetal element modulates its surface morphology, electronic structure, size of particles, and optical and physiochemical properties.[13] This nonmetal incorporation has an essential effect in tuning the band structure, extending absorption of visible irradiation and creating more active sites.[26]

One approach to solar light harvesting, namely, deposition of metal nanoparticles (NPs) exhibiting surface plasmon-induced effect (SPIE), has attracted great attention in the recent last years.[27–29] Among several metals used for driving SPIE effects in photocatalytic applications, Au and Ag are the most used due to their high-quality factors in the visible light.[27] Furthermore, Au NPs present the advantages of high inertness in numerous environments and easy surface modification. These interesting optical properties, coupled with catalytically active and redox-mediator properties, might yield beneficial effects on CO_2 photoreduction reactions.[3,30,31] Specifically, Au NPs can exhibit a broad surface plasmon band in the visible depending on several parameters such as average particles size and shape, interaction with the support, dielectric constant of the environment, etc. Due to earlier interest in Au NPs for catalysis applications, several methods for Au/TiO_2 and Au/C_3N_4 preparation are well described in the literature, such as deposition–precipitation, colloidal deposition, and impregnation–reduction.[32–35]

Here, we report a facile and one-step method for the preparation of (S, C, B)-doped g-C_3N_4/TiO_2 high surface area heterojunctions. A second-step deposition of Au NPs (<1 wt%) resulted in a three-component photocatalytic materials. Playing with the g-C_3N_4 doping element, the quality of the g-C_3N_4/TiO_2 heterojunction and the Au deposition specificity, allowed to tune CH_4 selectivity and productivity. The optimized Au/gC_3N_4-B/TiO_2 and Au/gC_3N_4-C/TiO_2 led, respectively, to total CH_4 selectivity and to a mean productivity rate of 8.5 μmol h^{-1} g^{-1} over at least 10h. To the best of our knowledge, this level of performance is unprecedented under continuous gas-phase flowing CO_2 in the presence of water vapor and under visible light irradiation, without addition of any sacrificial agent.

2. Results and Discussion

2.1. Thermal Stability (TGA)

TGA profiles of CN(–X), represented in **Figure 1**, top, show first a slight weight loss observed at roughly 200 °C, attributed to

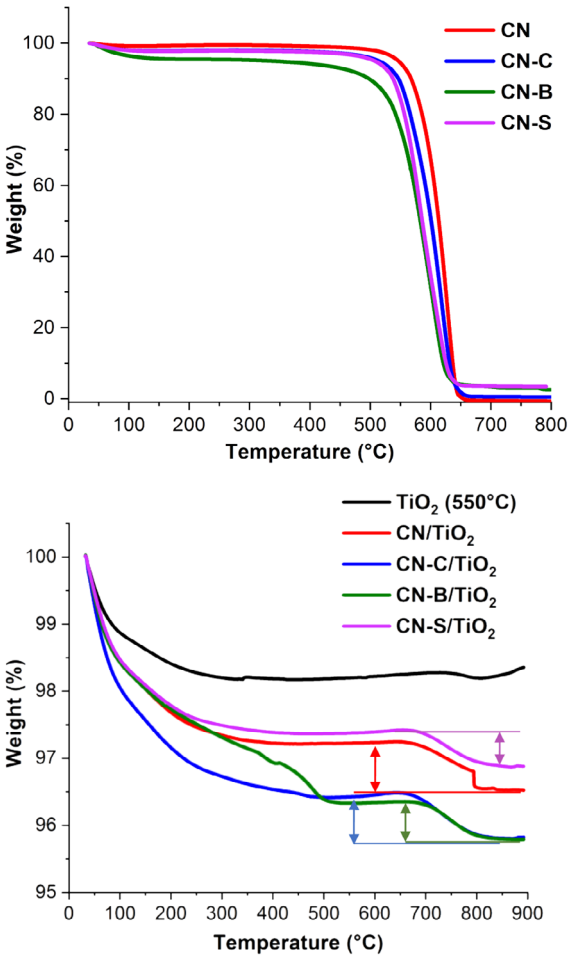

Figure 1. TGA analysis of (top) CN–X. (Bottom) CN(–X)/TiO_2 UV-100 compared to reference TiO_2 UV-100 (550 °C).

Table 1. TiO_2 anatase mean crystallite size (from XRD), doping element (B, S) content (wt%)*, and Au content (from ICP analyses).

–	Anatase mean cryst. size [nm]	B [wt%]	S [wt%]	g-C_3N_4 [wt% (exp)]	Au [wt% (exp)]
TiO_2 UV-100	9 ± 1	–	–	–	
Au/TiO_2 [550 °C]	18 ± 1	–	–	–	0.77 ± 0.01
Au/CN/TiO_2	15 ± 1	–	–	0.72 ± 0.01	0.77 ± 0.01
Au/CN–C/TiO_2	14 ± 1	–	–	0.59 ± 0.01	0.77 ± 0.01
Au/CN–B/TiO_2	15 ± 1	0.06 ± 0.01	–	0.55 ± 0.01	0.74 ± 0.01
Au/CN–S/TiO_2	15 ± 1	–	0.03 ± 0.01	0.54 ± 0.01	0.77 ± 0.01

elimination of adsorbed water,[36] followed by a classical and rapid one-pot decomposition starting at 550 °C and achieved at 650 °C, due to *s*-triazine or tris-*s*-triazine units burning.[37] Doping results in a slightly higher water elimination contribution and to a shift to lower temperatures for the beginning of decomposition (this phenomenon is a little bit more pronounced for B-doping for which the corresponding temperature is decreased to ≈460 °C), whereas the end of decomposition is quite not affected. These slight differences in terms of thermal stability may be attributed to different crystallinity/crystal thickness.[38]

From TGA analyses of CN(–X)/TiO_2 samples (Figure 1, bottom), one can deduce the g-C_3N_4 content (wt%) of the composite materials (**Table 1**). The first region of weight loss can be attributed to water molecules desorption and/or to TiO_2 dehydroxylation. One can, however, note that this first mass loss is more pronounced on CN–C-based composite. It must also be underlined that the total graphitic carbon nitride contents are low, between 0.54 and 0.72 wt%, whatever the samples. Although the presence of TiO_2 NPs on g-C_3N_4 generally lowers its temperature of combustion,[39] in our case, the association of TiO_2 and C_3N_4 somehow resulted in a drastic shift of the beginning of C_3N_4 decomposition toward higher temperatures, starting at ≈680 and 700 °C, respectively. The presence of TiO_2 thus prevents the 2D g-C_3N_4 structure from combustion. One can assume that this shift toward higher temperatures is due to strong interactions between TiO_2 NPs and graphitic carbon nitride sheets.

2.2. Structural Characterization (XRD)

The X-ray diffraction (XRD) pattern of the bare (uncalcined) TiO_2 UV-100 (Figure S2, top, Supporting Information) exhibited a major peak at 25.4° assigned to (101) planes of the anatase phase in agreement with JCPDS file 21-1276. Further treatment at 550 °C in air did not lead to the appearance of other crystallographic phases. However, an increase in crystallite mean particle size is observed (from 9 to 18 nm), due to sintering phenomena. One can mention that this sintering effect of TiO_2 crystallites is hindered within the composite materials during the synthesis and the formation of g-C_3N_4 nanosheets upon polycondensation at 550 °C, confirming strong interactions between both semiconductors even at those low graphitic carbon nitride contents, as previously observed.[40] As a result of the minor g-C_3N_4 content (max. 0.72 wt%), XRD patterns showed no obvious diffraction peak (Figure S2, Supporting Information) attributable to crystallized g-C_3N_4. This observation is in good agreement with other studies showing that at least 30 wt% of g-C_3N_4 is necessary to observe the corresponding diffraction lines in the XRD pattern of TiO_2-gC_3N_4 composites.[1,13] In the same manner, no diffraction peak related to crystallized Au was detected, resulting from too small Au loading (0.76 ± 0.02 wt%) and/or crystallite size (Figure S2, bottom, Supporting Information).

2.3. Surface Characterizations

2.3.1. BET Surface Area and Porosity Measurements

From BET measurements, one can observe that CN(–X) materials all exhibited type-II adsorption–desorption isotherms profiles (Figure S3, top, Supporting Information) related to macroporous solids with strong interactions between adsorbed nitrogen and the pores walls. They showed a large but monomodal pore size distribution (**Figure 2**) (as derived from Barrett, Joyner et Halenda (BJH) methods) centered at ≈33–38 nm, except for S-doped g-C_3N_4, which exhibited a somewhat larger mean pore diameter of ≈51 nm (**Figure 3**, top, Supporting Information). Bare g-C_3N_4 revealed the highest surface area of 171 $m^2 g^{-1}$, among all the studied samples, and the highest pore volume. Both surface areas and pore volume decreased upon doping

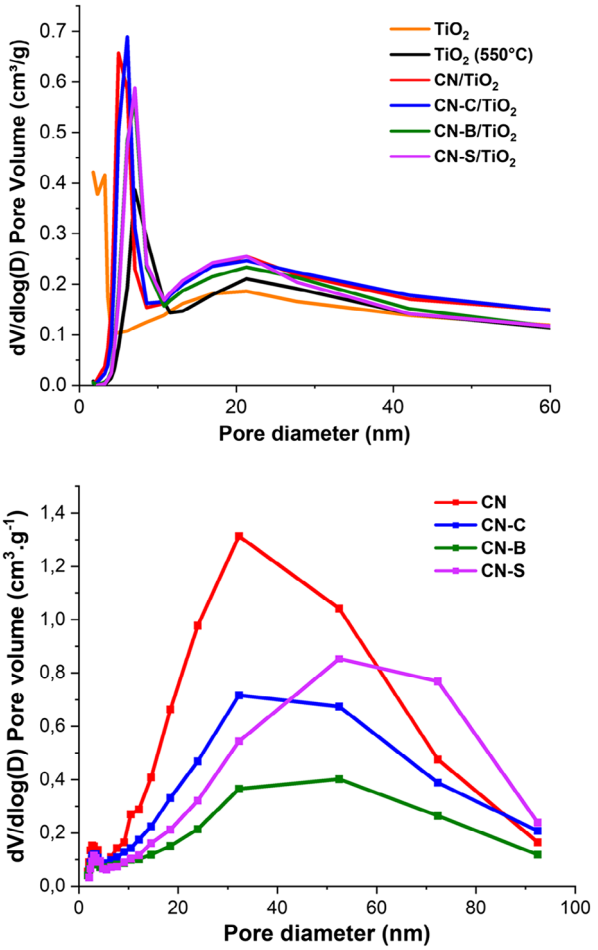

Figure 2. Mean pore size distribution of (top) CN–X samples. (Bottom) CN–X/TiO_2 and Au/TiO_2 UV-100 (550 °C) samples.

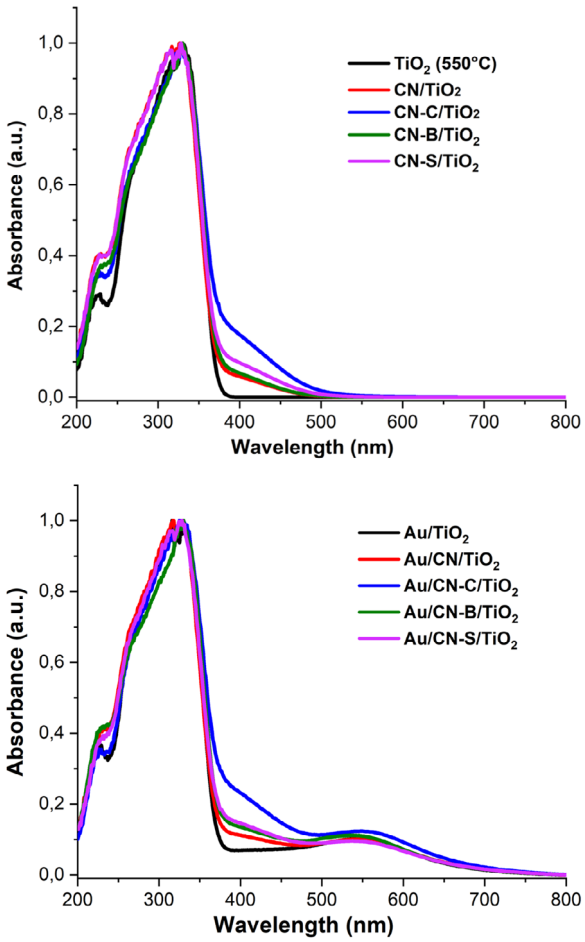

Figure 3. UV–vis absorbance spectra of (top) CN–X/TiO_2 and reference TiO_2 UV-100 (550 °C) (bottom) Au/CN–X/TiO_2 and Au/TiO_2 UV-100 (550 °C).

(**Table 2**). Among the different doped g-C_3N_4, S-doping yielded the largest pore volume and the most important surface area.

For the heterojunction materials, the coexistence of mesopores and macropores is observed (Table 2). Indeed, pore size distributions of all CN–X/TiO_2 composites exhibited a bimodal feature close to that observed by TiO_2 (550 °C). Adsorption–desorption isotherm profiles of the composites (Figure S3, bottom, Supporting Information) are also similar to that of TiO_2 (550 °C), showing that the morphology of the low loaded CN–X/TiO_2 heterojunction materials is determined by the major TiO_2 component. Variations in surface areas and pore volumes may thus be attributed to modifications in the principal TiO_2 component. It is interesting to highlight that surface areas and pore volumes of the heterojunctions are significantly higher than those expected from a mere linear combination of TiO_2 550 °C and CN–X considering their respective weight contents in the composite. This is consistent with inhibition of TiO_2 crystallite growth during CN–X polycondensation (as compared with the growth observed upon raw treatment of TiO_2 UV-100 in air at 550 °C), as shown by XRD.

More specifically, surface areas and pore volumes varied from $85 \pm 1\ m^2\ g^{-1}$ and $0.30\ cm^3\ g^{-1}$ for the B- and S-doped heterojunctions up to $112 \pm 7\ m^2\ g^{-1}$ and $0.35 \pm 0.01\ cm^3\ g^{-1}$ for the undoped and C-doped heterojunctions. This suggests that crystallization and growth of titania are impacted differently by the different conditions of polycondensation, i.e., the presence of the various dopants, and that the B and S-dopants are less efficient in controlling the growth of anatase during the polycondensation process.

2.3.2. UV–Vis Absorption Properties

CN–X/TiO_2 composite materials showed photon absorption contribution of both TiO_2 anatase and g-C_3N_4 counterparts, despite the very low content of this second semiconductor (**Figure 3** Top). One can observe that the second contribution is more or less pronounced depending on the nonmetal dopant. Doping of g-C_3N_4, except for B element, led to a displacement of the g-C_3N_4 absorption edge toward higher wavelengths, as confirmed by the lowering of bandgap value (Table 2), calculated from Tauc plot using Kubelka–Munk formula (Figure S4, Supporting Information). Furthermore, it is worthy to underline that C-doping resulted in a more intense redshift, and narrowing of the band gap (2.28 eV), followed by S- and B-doped-based C_3N_4. The presence of Au NPs is evidenced by the characteristic surface plasmon resonance (SPR) contribution centered at ≈550 nm (Figure 3, bottom).

Table 2. Bandgap values, surface area, total pore volume, and mean pore size diameter.

–	E_{g1} [eV] (TiO_2)	E_{g2} [eV] CN(–X)	S_{BET} [$m^2\ g^{-1}$]	V_{pore} [$cm^3\ g^{-1}$]	Mean pore diameter [nm]
TiO_2 UV-100	3.25 ± 0.02	–	315 ± 10	0.33 ± 0.05	2–3
TiO_2 [550 °C]	3.20 ± 0.02	–	65 ± 2	0.24 ± 0.02	7–21
CN	–	2.83 ± 0.02	171 ± 3	0.94± 0.04	33
CN/TiO_2	3.17 ± 0.02	2.35 ± 0.02	119 ± 2	0.36 ± 0.02	5–21
CN–C	–	2.58 ± 0.02	115 ± 2	0.56 ± 0.02	33
CN–C/TiO_2	3.12 ± 0.02	2.28 ± 0.02	105 ± 2	0.34 ± 0.02	6–21
CN–B	–	2.78 ± 0.02	104 ± 2	0.54 ± 0.03	38
CN–B/TiO_2	3.15 ± 0.02	2.34 ± 0.02	84 ± 2	0.29 ± 0.02	7–21
CN–S	–	2.65 ± 0.02	136 ± 2	0.62 ± 0.02	51
CN–S/TiO_2	3.12 ± 0.02	2.30 ± 0.02	86 ± 2	0.30 ± 0.02	7–21

The position of the SPR peak is not really affected by the nature of the g-C_3N_4 support. This is consistent with the similar size ranges of Au NPs produced on the different supports (≈3 nm, **Figure 4**) and their supposed similar interactions with the support. Only the Au/CN–C/TiO_2 sample seemed to show slight shift in the position of the SPR. Moreover, one can also

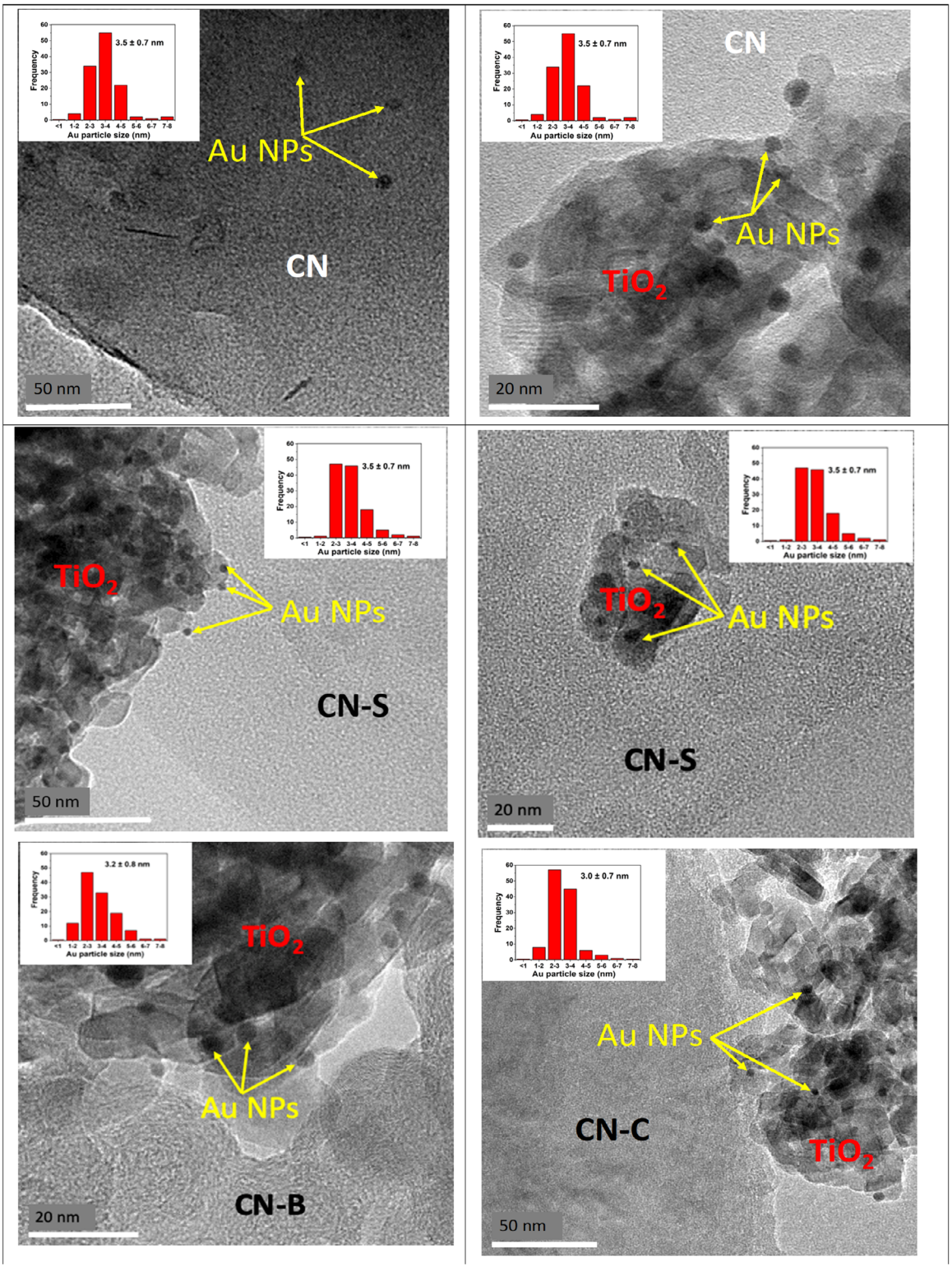

Figure 4. TEM micrographs of (top) Au/CN/TiO_2, (middle) Au/CN–S/TiO_2, (bottom left) Au/CN–B/TiO_2, and (bottom right) Au/CN–C/TiO_2.

mention that the intensity of the SPR peak is the same whatever the samples, confirming the same Au loading. It is worthy to underline the overlap between the g-C_3N_4 and Au SPR absorption windows that might be beneficial for increased visible light photons absorption by the former SC, due to energy transfers related to electromagnetic field enhancement around Au NPs.[41]

2.3.3. TEM Characterization

Figure 4 presents TEM images of Au/CN(–X)/TiO_2 nanocomposites. One can highlight that on Au/CN–X/TiO_2 composites (Figure 4, middle and bottom), Au NPs are quite exclusively deposited onto TiO_2 surfaces, scarcely on CN ones and none on CN–X ones. This observation can easily be explained considering the very low concentration of CN–(X) sheets, consequently leading to very low probability of contact between Au precursor and those surfaces. In all cases, the mean Au NPs size is ≈3.0–3.5 nm, noting, however, that the distribution is the narrowest on Au/CN–C/TiO_2 material, confirming probably the slight shift in SPR position observed from UV–vis absorbance measurements. One can also mention that B–gC_3N_4 showed particular morphology of rolled up nanosheets (≈10 sheets) well interfaced with Au/TiO_2 material.

2.3.4. Photocatalytic Performances

Under artificial visible light irradiation, exclusively H_2 and CH_4 were produced (**Table 3**) in the gas phase. First, one can mention that quite no activity is observed without Au NPs deposition, clearly meaning that the visible light CO_2 photoreduction activity is induced by the presence of Au. Only the CN–C/TiO_2 heterojunction led to the formation of some hydrogen, showing some photocatalytic activity in the absence of Au, but no methane production. Au NPs deposition resulted in increasing the photoreduction activity in a more or less pronounced way, and increased the selectivity of CN–C/TiO_2 toward methane. It must be underlined that the reference Au/CN photocatalyst was inactive toward CO_2 photoreduction under visible light activation conditions (not shown), whereas the reference Au/TiO_2 exhibited low activity, mainly selective toward H_2 production. Looking at the Au/CN/TiO_2 undoped composite, its activity was enhanced compared to its reference counterparts, but its selectivity for methane production remained low. Contrarily, the doped Au/CN–X/TiO_2 composite photocatalysts appeared highly selective toward CH_4 production. Both Au/CN–B/TiO_2 and Au/CN–S/TiO_2 samples reached total methane selectivity. Furthermore, Au/CN–B/TiO_2 composite led to the highest methane productivity (4.49 μmol h^{-1} g^{-1}), which is, to the best of our knowledge, one of the best performances reported up to now in the literature under visible light irradiation under similar experimental conditions. The Au/CN–C/TiO_2 nanocomposite led both to the highest activity and CH_4 formation rate of 8.49 μmol h^{-1} g^{-1} under visible light activation. Hence, the Au/CN–X/TiO_2 three-component system allowed to considerably increase CH_4 selectivity and to reach total selectivity with the boron and sulfur dopants. From **Figure 5** showing the evolution of CH_4 (top) and H_2 (bottom) products as a function of time under continuous CO_2/H_2O flow, it can be observed that

Table 3. Average production rate and electronic selectivity (over 10 h of continuous reaction) in the presence of water vapor ($CO_2/H_2O = 96/4$ mol. ratio) at 0.3 mL min^{-1} continuous flow under visible light irradiation.

–	Products	r_{10h} [μmol h^{-1} g^{-1}]	Selectivity [%]
TiO_2 [550 °C]	H_2	0	0
	CH_4	0.06	100
Au/TiO_2 [550 °C]	H_2	0.81	87
	CH_4	0.25	13
CN/TiO_2	H_2	0	0
	CH_4	0.09	100
CN–C/TiO_2	H_2	0.38	100
	CH_4	0.00	0
CN–B/TiO_2	H_2	0.00	0
	CH_4	0.03	100
CN–S/TiO_2	H_2	0.00	0
	CH_4	0.25	100
Au/CN/TiO_2	H_2	2.09	95
	CH_4	0.04	5
Au/CN–C/TiO_2	H_2	1.93	5
	CH_4	8.49	95
Au/CN–B/TiO_2	H_2	0	0
	CH_4	2.01	100
Au/CN–S/TiO_2	H_2	0	0
	CH_4	0.42	100

Au/CN–C/TiO_2 sample followed a typical trend with an increase of production in the first 150 min to reach a maximum, followed by deactivation, as observed before on solar Au/TiO_2 photocatalysts.[42] However, the fully selective Au/CN–B/TiO_2 photocatalyst did not exhibit this deactivation phenomenon; it produced continuous high-level CH_4 production over at least the 10 h of tests.

2.3.5. TRMC

The lifetime of charge carriers is completely described by the whole TRMC decay (I(t)).[31,32] This decay is complex and may be due to different mechanisms that governs free electron mobility (considered as the most mobile photogenerated charge carriers on TiO_2- and CN-based materials), like recombination and trapping. Different features can be observed at the different excitation wavelengths. From **Figure 6**, top left, one can see, comparing the two commercially available TiO_2 P25 and TiO_2 UV-100, that the last one allowed slightly larger initial charge-carrier formation but more rapid free electrons loss of mobility. Contrarily to what is generally observed, the deposition of Au NPs maintains this large density of charge-carrier generation while enhancing considerably electron mobility, probably by acting as electron traps and thus hindering charge-carrier recombination. Exciting the metal-free TiO_2 and CN (CN–C) reference supports at 450 nm (Figure 6, middle left) did not lead to significant charge-carrier production. However, one can underline that the association of TiO_2 (UV-100) to CN or CN–C boosted the

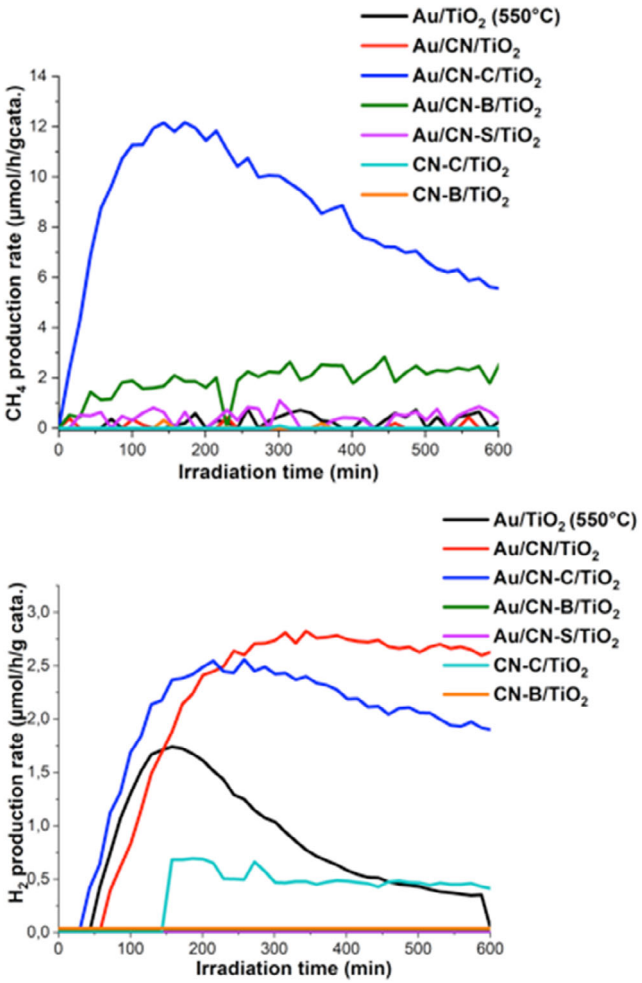

Figure 5. Specific CH_4 (top) and (bottom) H_2 production rates in presence water vapor ($CO_2/H_2O = 96/4$ mol. ratio) at 0.3 mL min^{-1} continuous flow under visible light irradiation.

generation of "visible light-activated" charge carrier, assuming carbon nitride-driven visible light photosensitization. More interestingly, the decay of free electron mobility is more important in the case of carbon doping, suggesting a less effective e–hole pairs separation onto the CN–C/TiO_2 heterojunction. Au NPs deposition (Figure 6, middle right) damps the initial TRMC signal in a more or less pronounced way depending on the support, probably due to electron trapping effects of Au NPs. Nevertheless, it is worthy to highlight that this initial signal drastically decreased on TiO_2 support. It decreased less on Au/CN/TiO_2 and even less on the CN–C/TiO_2 heterojunction, for which damping of the TRMC signal by Au NPs was quite limited. One may assume in this last case that this most efficient charge-carrier generation may be associated to possible favorable field enhancement effect that counterbalances the negative electron trapping effect by Au NPs. Furthermore, this positive effect is enhanced onto the CN–C/TiO_2 heterojunction, thanks to its higher absorbance in the 450-500 nm range (Figure 3). At 550 nm, as shown in Figure 6, bottom left, one can see small charge-carrier generation but only on TiO_2 and CN(CN–C)/TiO_2 heterojunction, nothing is detected on CN or (CN–C) reference samples. One may also have assigned this observation to carbon nitride-driven sensitization, which phenomenon was, however, more attenuated at 550 nm than at 450 nm, possibly due to the negligible absorbance of the heterojunctions above 550 nm (Figure 3, top). Under these conditions, addition of Au NPs decreased the signal intensity, certainly resulting from trapping effect of Au NPs. Comparing the signals of the photocatalytic composite material Au/CN–C/TiO_2, which exhibited the most important CH_4 productivity, at 450 and 550 nm (after normalization, taking into account the energy received at different wavelength pulses) showed that even if a large signal is observed at 450 nm, no charge-carrier production occurred at 550 nm. This observation supports the assumption that the electron trap effect is predominant compared to the SPIE one due to the fact that the possible near-field intensification around Au NPs cannot be used by the heterojunction at this wavelength.

Summarizing the TRMC behaviors in correlation with the abovementioned performed characterizations (TGA, XRD, UV–vis, TEM) allows us to explain the best performance of the Au/CN–C/TiO_2 composite photocatalyst and to propose schematic charge-carrier and reaction pathways (**Figure 7**). First, the more extended visible light harvesting (absorption tail up to 550 nm, evidenced by UV–vis absorbance measurements) resulted in more extended visible light sensitization, due to strong and high-quality interactions between both kinds of nanocomponents. Second, it has already been reported that citric acid-added urea synthesis for obtaining C-doped g-C_3N_4 yielded the formation of few loaded N-doped graphitic carbon units in g-C_3N_4 matrix, but too small to be detected with certainty using ICP, XRD, UV–vis, and TEM analyses.[43] This kind of carbon doping may allow enhanced electron delocalization onto some N-doped graphitic carbon units and thus better charge-carrier separation. Third, Au NPs mainly acted as electron trapping/cocatalytic function for CO_2 reduction; however, plasmonic effects cannot be excluded for Au/CN–C/TiO_2; indeed, the limited electron trapping effect observed for Au/CN–C/TiO_2 composite, compared to undoped CN-containing photocatalyst, could result from a counterbalancing field enhancement effect. In addition to the aforementioned impacting criteria, one can also assume that CN doping, along with the lowering of band gap energy, may also modify CO_2 adsorption. Optimized design of the band edge(s) position probably lowered the one of the conduction band. As a consequence, the electrons located onto the conduction band of doped CN became less energetic toward H_2 reduction half-reaction. In parallel, as CO_2 adsorption most probably takes place onto Au/TiO_2 surfaces, CO_2 reduction half-reaction can thus easily be carried out, thanks to the electrons initially photogenerated onto doped CN and transferred from its conduction band to that of TiO_2.[44] CO_2 adsorption on the CN–X component can, however, not be ruled out. CO_2 adsorption has indeed been reported to be facilitated on, e.g., B-doped C_3N_4 (as compared to undoped CN) which may also contribute to the observed optimized performances of the Au/CN–X/TiO_2 composites. Nevertheless, the BET surface areas, in the 90–120 $m^2 g^{-1}$ range, seemed not to be an impacting factor for visible light-driven gas-phase photocatalytic CO_2 reduction in presence of H_2O.

The most performing spent photocatalysts (Au/CN–C/TiO_2 and Au/CN–B/TiO_2) have also been characterized by means

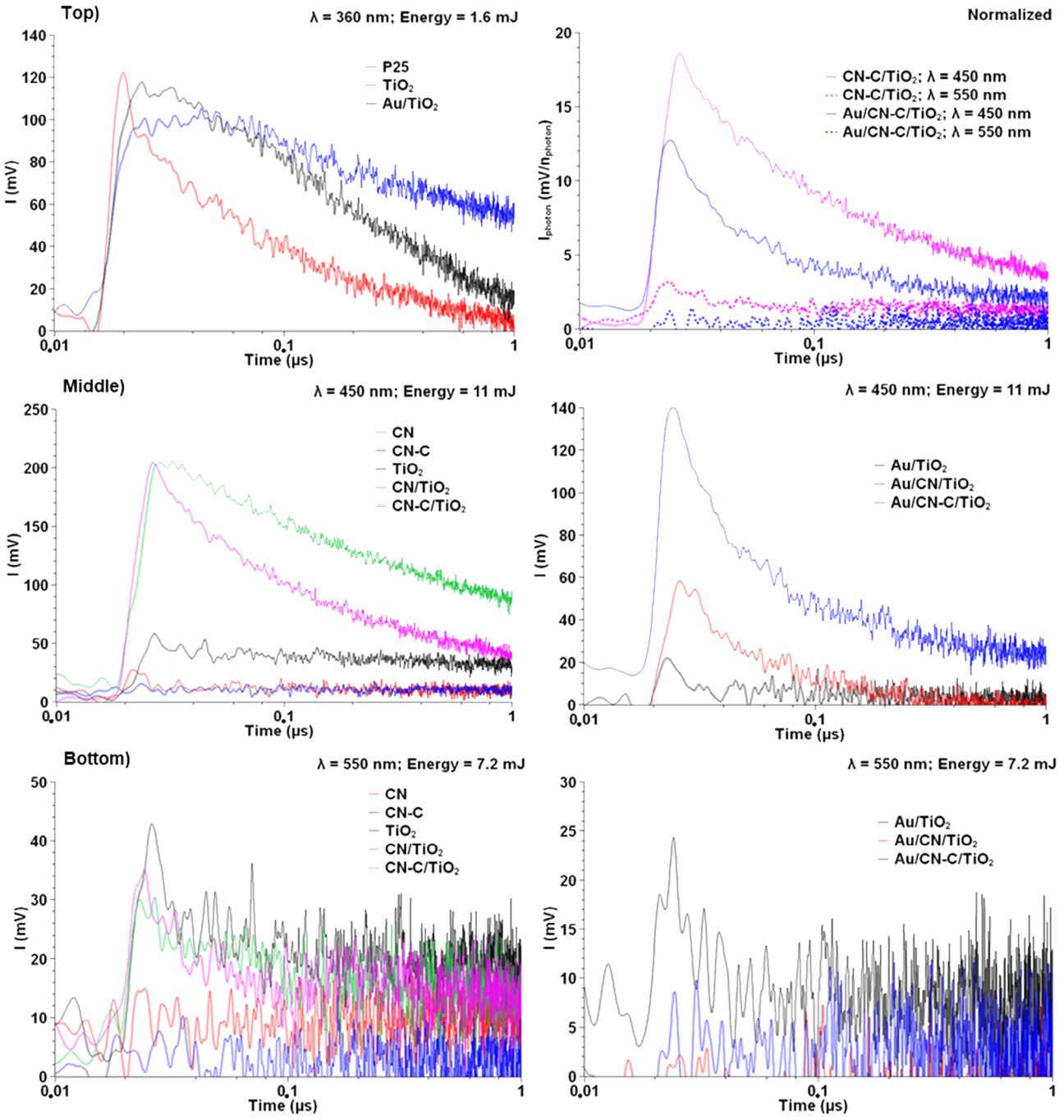

Figure 6. TRMC measurements obtained at (top left) 360 nm, (middle) 450 nm, (bottom) 550 nm, and (bottom right) 550 nm. (Top right) Normalized signals compared at 450 and 550 nm.

of structural (XRD, Figure S5, Supporting Information), surface (X-ray photoemission spectroscopy (XPS), Figure S6, Supporting Information), and optical (UV–vis absorbance, Figure S7, Supporting Information) analyses and compared to the fresh samples. It is clearly evidenced that no structural modification occurred during photocatalysis. Looking at XPS surface analyses, mainly dominated by typical TiO_2 behaviors, one can observe that neither carbon, titanium, oxygen, gold, nor boron surface species were affected by the photocatalytic tests. Considering light absorption properties, one can, however, mention that the Au/CN–C/TiO_2 samples, exhibiting initially the more extended visible light absorption properties, were slightly affected by reducing its visible light absorption capacity; one can thus assume that carbon-doping species, mainly located inside the porosity of the material, slightly lose their stability under photocatalytic conditions.

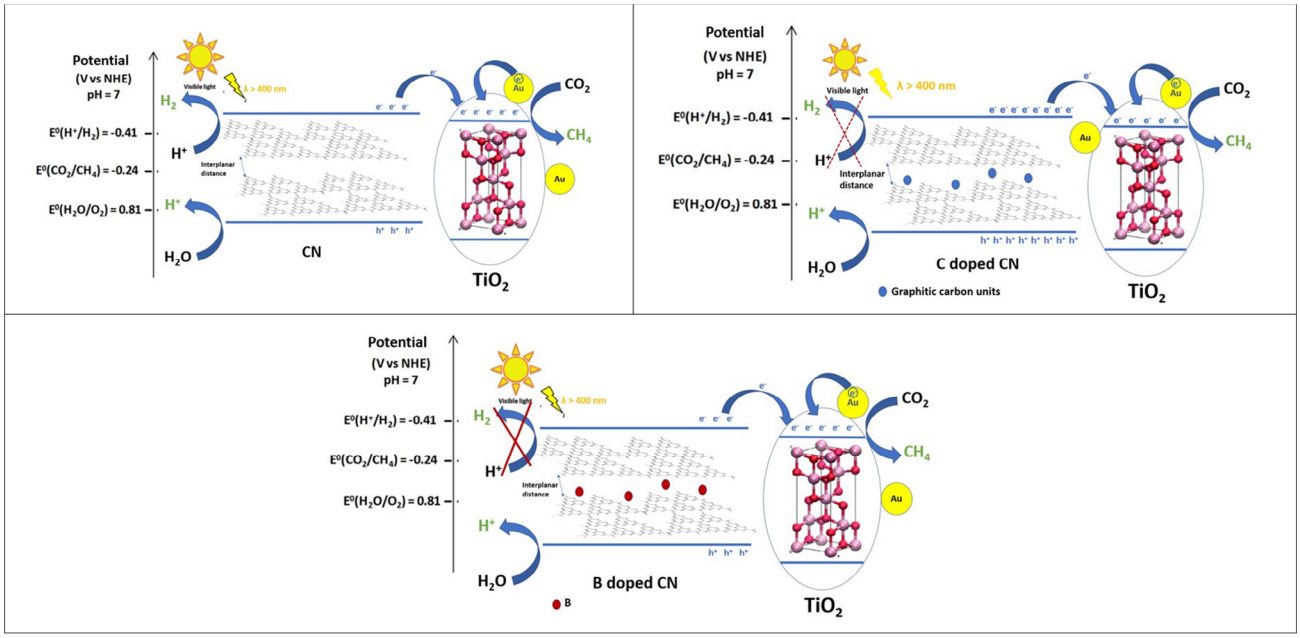

Figure 7. Schematic charge-carrier and reaction pathways on (top left) Au/CN/TiO_2, (top right) Au/CN–C/TiO_2, and (bottom) Au/CN–B/TiO_2.

3. Conclusion

In this article, we succeeded in tuning visible light-driven gas-phase photocatalytic CO_2 reduction into CH_4 by designing optimized three-component Au/doped C_3N_4/TiO_2 composite photocatalysts. The strategy consisted in associating low containing doped graphitic carbon nitride to commercially available TiO_2 UV-100, leading to the formation of high-quality heterojunction with strong interactions between the two components. Namely, B- and C-doping were obtained by introducing the corresponding doping element precursors with urea, in the presence of suspended TiO_2, before thermal polycondensation. The resulting doped g-C_3N_4 material exhibited enhanced visible light harvesting properties, especially in the case of C-doping. Further deposition of small Au NPs (≈3 nm), quite exclusively onto TiO_2 surfaces, acted as electron trapping/cocatalytic functions. Depending on the activation wavelength, surface plasmonic effects could also contribute to the photocatalytic activity, especially in the 400-500 nm range. In addition, it was assumed that B– and C–C_3N_4 doping, leading to a more or less low conduction band position, was the impacting factor toward total CH_4 selectivity. The (0.77 wt%)Au/(0.59 wt%)C–C_3N_4/TiO_2 composite photocatalyst, exhibiting the best compromise between those various impacting factors, led to a continuous productivity rate of CH_4 of 8.5 μmol h^{-1} g^{-1} over at least 10 h. To the best of our knowledge, this level of performance is unprecedented under continuous gas phase flowing CO_2.

4. Experimental Section

Materials: Urea (NH_2CONH_2, 99%, Sigma–Aldrich), citric acid monohydrate ($(HOC(COOH)CH_2COOH)_2.H_2O$, ≥99%, Sigma–Aldrich), boric acid (H_3BO_3, ≥99.5%, Sigma–Aldrich), chloroauric acid ($HAu^{III}Cl_4.3H_2O$) (≥99.9% trace metal basic, Alfa Aesar), sodium borohydride (≥98%, Sigma–Aldrich), ethanol (CH_3CH_2OH, ≥96%, Sigma–Aldrich), triethanolamine (TEOA, ≥ 99%, Sigma–Aldrich), and 2-thiobarbituric acid ($C_4H_4N_2O_2S$, ≥98%, Sigma–Aldrich) were used without further purification. TiO_2 Hombikat UV-100 (anatase > 250 m^2 g^{-1}) was purchased from Sachtleben Chemie GmbH and used without further purification.

Synthesis of (Doped) g-C3N4 and TiO2/(Doped) g-C3N4-Based Materials: Pure g-C_3N_4 was synthesized via thermal polycondensation of urea at 550 °C for 3 h, with a heating ramp rate of 15 °C min^{-1}. 10 g of urea was put into an alumina crucible with a top cover, resulting in ≈0.25 g of g-C_3N_4. The obtained product is denoted as CN. The nonmetal doped g-C_3N_4 was synthesized by mixing urea (10 g) and 10 mg of the precursor of nonmetal elements (H_3BO_3 for element B, $HOC(COOH)CH_2COOH)_2.H_2O$ (acetic acid) for element C and $C_4H_4N_2O_2S$ (2-thiobarbituric acid) for element S. After grinding, the mixture was annealed at 550 °C for 3 h in a muffle furnace. The samples were named as CN–X, where X is the dopant element (C, B, or S) in g-C_3N_4.

The TiO_2/g-C_3N_4 heterojunctions were prepared by wet impregnation of 10 g of the urea precursor onto 2 g of TiO_2 in suspension in 20 mL of distilled water at 40 °C, followed by evaporation of the solvent under magnetic stirring. The obtained materials were named CN/TiO_2. Alternatively, the TiO_2/(doped)g-C_3N_4 heterojunctions were obtained by mixing at the same time 10 mg of the abovementioned precursors of nonmetal elements with the 10 mg of urea during the wet impregnation step, and named CN–X/TiO_2 (with X = C, B, or S). For reference, TiO_2 UV-100 was submitted to the same experimental conditions (at 550 °C) than for polycondensation reaction; the resulting material was labeled TiO_2 (550 °C).

Deposition of Au NPs Onto TiO2/(Doped) g-C3N4 Materials: Au (0.86 wt% theoretical value) was loaded onto the surface of CN(–X)/TiO_2 samples by an impregnation–reduction method[35,42,45] using $HAu^{III}Cl_4$ as the precursor of gold. In a 100 mL flask, 40 mL of H_2O, 80 mL of $HAu^{III}Cl_4.3H_2O$ (0.22 M in water), and 400 mg of C_3N_4 were mixed. The whole is left under a magnetic stirrer (1000 rpm) for 45 min while the precursor is impregnated. Then 1 mL of a solution of $NaBH_4$ (0.1 M) was added (with $NaBH_4$/metal precursor = 5) to the freshly prepared mixture. A gray coloration which highlights the reduction of Au NPs is observed. After the reduction, the mixture is stirred for 15 min and then the obtained material is filtered and washed with 1 L of distilled water. During filtration, the filtrate

appears clear and colorless, which suggests that a good deposit has been obtained. Finally, the composite is placed in an oven at 100 °C for 24 h; a gray powder of Au-based material is obtained. By inductively coupled plasma atomic emission spectroscopy (ICP-AES) analysis, it was confirmed that the deposition yields of Au NPs were around 89%, leading to an actual Au loading of 0.76 ± 0.02%. The resulting samples are labeled Au/CN–X/TiO_2.

Materials Characterization: Elemental analyses of the composites were performed using ICP-AES. The limit of detection of the instrument is 0.1 mg L^{-1} for Au. Analysis of the Au component of the nanocomposites allowed us to calculate deposition yields which are defined as the ratio between the real deposited mass of Au (deduced from ICP-AES analysis) and the mass of Au introduced during deposition step.

Thermogravimetric (TGA) analyses were performed using a model Q 5000 IR apparatus from TA Instrument equipped with a sample changer and a microbalance with a sensitivity of around 0.1 mg. 3 mg of each sample was placed in a platinum crucible, and then heated from room temperature to a temperature of 800 °C with a temperature rise ramp of 15 °C min^{-1} under an air flow rate of 25 mL min^{-1}. Standard deviation on the decomposition temperature of the as-prepared samples is ±10 °C.

The X-Ray diffraction apparatus used is a Bruker D8 Advance diffractometer equipped with a Lynxeye XE detector operating at 40 kV and 40 mA in θ/θ mode. The source of the X-rays is a copper anticathode using the Kα line at 1.5418 Å. In order to obtain normalized diffractograms, a fixed amount of 50 mg of the sample was placed on a plastic holder. The acquisition of diffractograms was performed in scanning mode in steps of $2\theta = 10°$ to $2\theta = 38°$ with a step of 0.041 and a counting time of 5 s per step. The mean crystal thickness is calculated from the Debye–Scherrer equation based on the width at half maximum and the position of the most intense peak.

The nitrogen adsorption–desorption isotherms were obtained using a Micromeritics Asap 2420 porosimeter. The analysis is carried out under atmospheric pressure at the nitrogen liquefaction temperature (−196 °C). The materials were degassed at 150 °C under primary vacuum for 8 h with a temperature rise of 10 °C min^{-1} in order to desorb water and adsorbed molecules from their surfaces. The specific surfaces of the materials were calculated from the adsorption isotherm by the Brunauer–Emmett–Teller (BET) method. From the desorption, the pore size distribution can be calculated by the BJH method specifically for mesoporous solids.

High-resolution transmission electron microscopy (HRTEM) was performed on a Jeol 2100 F microscope equipped with a lanthanum hexaboride cathode (LaB6) operating at 200 kV. The sample was sonicated in ethanol and then a drop of the suspension is placed on a carbon membrane placed on a copper grid. HRTEM is used to determine the size of Au NPs and consequently the distribution in size is obtained by measuring the particles size for more than 100 particles using the ImageJ software [W. Rasband, http://rsb.info.nih.gov/ij/]. UV–vis absorption spectra were recorded on a Perkin Elmer 950 spectrophotometer fitted with a Labsphere RSA ASSY 100 nm integrating sphere. The spectra are acquired in reflection mode (diffuse reflectance). In order to determine the absorbance coefficient, the diffuse reflectance spectra were converted to Kubelka–Munk units via the equation: $F(R) = \frac{(1-R)^2}{2R}$. To obtain the bandgap (E_g) of the semiconductor (SC), the Tauc equation $(F(R)*h\nu)^S = (h\nu - E_g)$ was used where h is the Planck constant, ν is the frequency, and S is a coefficient which is 1/2 in the case of an SC indirect gap (TiO_2) and 2 in the case of a direct band gap SC (for bulk g-C_3N_4). However, nanosheet-based g-C_3N_4 has been reported as having an indirect gap with the corresponding S coefficient being 1/2.[46]

The charge-carrier lifetimes in TiO_2 after UV illumination were determined by microwave absorption experiments using the time-resolved microwave conductivity method (TRMC).[42,47] The TRMC technique is based on the measurement of the change of the microwave power reflected by a sample, $\Delta P(t)$, induced by its laser pulsed illumination. The relative difference $\Delta P(t)/P$ can be correlated, for small perturbations of conductivity, to the difference of the conductivity $\Delta\sigma(t)$ considering the following equation

$$\frac{\Delta P(t)}{P} = A\Delta\sigma(t) = Ae\sum_i \Delta n_i(t)\mu_i \quad (1)$$

where $\Delta n_i(t)$ is the number of excess charge-carrier i at time t and μ_i their mobility. The sensitivity factor A is independent of time, but depends on different factors such as the microwave frequency or the dielectric constant. Considering that the trapped species have a small mobility, which can be neglected, Δn_i is reduced to mobile electrons in the conduction band and holes in the valence band. And in the specific case of TiO_2 and g-C_3N_4, the TRMC signal can be attributed to electrons because their mobility is much larger than that of the holes. The incident microwaves were generated by a Gunn diode of the K_α band at 30 GHz. Pulsed light source was an OPO laser (EKSPLA, NT342B) tunable from 225 to 2000 nm. It delivers 8 ns full width at half maximum pulses with a frequency of 10 Hz. The light energy densities received by the sample were 1.6, 11, and 7.2 mJ at 360, 450, and 550 nm, respectively. Each measurement has been repeated two times. The main data provided by TRMC are the maximum value of the signal (I_{max}), which indicates the number of the excess charge carriers created by the pulse, including decay processes during the excitation by the laser (10 ns), and the decay ($I(t)$) due to the decrease of the excess electrons, either by recombination or trapping processes.

Photocatalytic Tests: Photocatalytic setup has already been described in detail elsewhere.[48] During the test, continuous flowing reaction mixture ($CO_2 + H_2O$, $CO_2/H_2O = 96/4$) flow (0.3 mL min^{-1}) passes through a light-transparent photoreactor (6 mL) equipped with a Hg lamp simulating artificial solar light (150 W ceramic–metal–halide Hg lamp). Total photon flux for the whole lamp spectrum is 0.028 and 0.024 mol s^{-1} m^{-2} for visible light irradiance after applying a filter cutting $\lambda < 400$ nm (Figure S1, Supporting Information). The irradiated surface is 19.65 cm^2. For photocatalytic tests, 50 mg of materials are dispersed in ethanol and deposited on a 50 mm diameter glass disk by evaporation at 100 °C. The surface concentration of photocatalyst on the glass disc is 25 g m^{-2}. The glass disk is then put in the reactor and the pilot is purged for 5 min with CO_2 flow (>100 mL min^{-1}) to remove air and other gas impurities. As a blank test, the setup is running without CO_2 gas flow under illumination to control the absence of gaseous products that may be the result of carbon-based contaminants conversion.[49]. Products from the reactor are analyzed by an online micro-GC (Agilent 3000A SRA instrument, Molsieve MS5A columns). Finally, the lamp is switched on and the duration of test is 10 h. Production rates were calculated according to the following equations

$$r_X(\text{mol h}^{-1}\text{g}^{-1}) = \frac{[X] \times 10^{-6} \times (\text{flow rate}) \times 60}{V_m \times m_{\text{photocat}}} \quad (2)$$

where [X] is the concentration in ppm, m_{photocat} is the mass of photocatalyst, $S_{\text{irradiated}}$ is the irradiated surface (0.001965 m^2), and the flow rate is 0.0003 L min^{-1} and $V_m = 24.79$ L mol^{-1} (STP conditions).

Electronic selectivity was calculated by these equations

$$\text{CH}_4 \text{ Selectivity} = \frac{8\,[\text{CH}_4]}{8\,[\text{CH}_4] + 2\,[\text{H}_2]} \quad (3)$$

$$\text{H}_2 \text{ Selectivity} = 1 - \text{CH}_4 \text{ Selectivity} \quad (4)$$

Supporting Information

Supporting Information is available from the Wiley Online Library or from the author.

Conflict of Interest

The authors declare no conflict of interest.

Data Availability Statement

The data that support the findings of this study are available from the corresponding author upon reasonable request.

Keywords

CH_4 productivity, CO_2 reduction, doped gC_3N_4/TiO_2 heterojunctions, photocatalysis

Received: March 26, 2023
Revised: June 15, 2023
Published online: August 28, 2023

[1] S. N. Habisreutinger, L. Schmidt-Mende, J. K. Stolarczyk, *Angew. Chem. Int. Ed.* **2013**, *52*, 7372.
[2] K. Li, X. An, K. H. Park, M. Khraisheh, J. Tang, *Catal. Today* **2014**, *224*, 3.
[3] B. T. Barrocas, N. Ambrozova, K. Koci, *Materials* **2022**, *15*, 967.
[4] T. Inoue, A. Fushishima, S. Konishi, K. Honda, *Nature* **1979**, *277*, 637.
[5] S. Neatu, J. A. Macia-Agullo, H. Garcia, *Int. J. Mol. Sci.* **2014**, *15*, 5246.
[6] J. Ran, M. Jaroniec, S. Z. Qiao, *Adv. Mater.* **2018**, *30*, 1704649.
[7] S. Xie, Q. Zhang, G. Liu, Y. Wang, *Chem. Commun.* **2015**, *1*.
[8] U. Aslam, V. G. Rao, S. Linic, *Nat. Catal.* **2018**, *1*, 656.
[9] A. Dhakshinamoorthy, S. Navalon, A. Corma, H. Garcia, *Energy Environ. Sci.* **2012**, *5*, 9217.
[10] L. Wei, C. Yu, Q. Zhang, H. Liu, Y. Wang, *J. Mater. Chem. A* **2018**, *6*, 22411.
[11] M. Reli, P. Huo, M. Sihor, N. Ambrozova, I. Troppova, L. Matejova, J. Lang, L. Svoboda, P. Kuztrowski, M. Ritz, P. Praus, K. Koci, *J. Phys. Chem. A* **2016**, *120*, 8564.
[12] C. Marchal, T. Cottineau, M. G. Mendez-Medrano, C. Colbeau-Justin, V. Caps, V. Keller, *Adv. Energy Mater.* **2018**, 1702142.
[13] S. Zhou, Y. Liu, J. Li, Y. Wang, G. Jiang, Z. Zhao, D. Wang, A. Duan, J. Liu, Y. Wei, *Appl. Catal. B* **2014**, *158–159*, 20.
[14] M. Tahir, B. Tahir, *Chem. Eng. J.* **2020**, *400*, 125868.
[15] L. Kong, J. Wang, F. Ma, M. Sun, J. Quan, *Appl. Mater. Today* **2019**, *16*, 388.
[16] W.-J. Ong, L.-L. Tan, S.-T. Yong, S.-P. Chai, *Chem. Rev.* **2016**, *116*, 7159.
[17] M. Tahir, B. Tahir, *J. Mat. Sci. Tech.* **2022**, *106*, 195.
[18] K. Wang, J. Fu, Y. Zheng, *Appl. Catal. B* **2019**, *254*, 270.
[19] S. W. Cao, H. Li, T. Tong, H. C. Chen, A. C. Yu, J. G. Yu, H. M. Chen, *Adv. Funct. Mater.* **2018**, *28*, 1870224.
[20] X. C. Wang, S. Blechert, M. Antonietti, *ACS Catal.* **2012**, *2*, 1596.
[21] J. Yu, S. Wang, J. Low, W. Xiao, *Phys. Chem. Chem. Phys.* **2013**, *15*, 16883.
[22] H. Zhang, A. Du, N. S. Gandhi, Y. Jiao, Y. Zhang, X. Lin, X. Lu, Y. Tang, *App. Surf. Sci.* **2018**, *455*, 1116.
[23] J. Xu, L. Zhang, R. Shi, Y. Zhu, *J. Mater. Chem. A* **2013**, *1*, 14766.
[24] J. Wang, J. Cong, H. Xu, J. Wang, H. Liu, M. Liang, J. Gao, Q. Ni, J. Yao, *ACS Sust. Chem. Eng.* **2017**, *5*, 10633.
[25] F. Wang, W. Lei, X. Pan, Z. Ye, *Nanotechnology* **2020**, *31*, 475406.
[26] D. Long, L. Wang, H. Cai, X. Rao, Y. Zhang, *Catal. Lett.* **2020**, *150*, 2487.
[27] Y. Zhang, S. He, W. Guo, Y. Hu, J. Huang, J. R. Mulcahy, *Chem. Rev.* **2018**, *118*, 2927.
[28] S. Kim, J.-M. Kim, J.-E. Park, J.-M. Nam, *Adv. Mater.* **2018**, 1704528.
[29] S. Linic, U. Aslam, C. Boerigter, M. Morabito, *Nat. Mater.* **2015**, *14*, 567.
[30] D. Glass, R. Quesada-Cabrera, S. Bardey, P. Promdet, R. Sapienza, V. Keller, S. A. Meier, V. Caps, I. P. Parkin, E. Cortés, *ACS Energy Lett.* **2021**, *6*, 4273.
[31] P. Jimenez-Calvo, V. Caps, V. Keller, *Renewable Sustainable Energy Rev.* **2021**, *149*, 111095.
[32] M. Haruta, *Gold Bull.* **2004**, *37*, 27.
[33] F. Vigneron, V. Caps, *CR Chimie* **2016**, *19*, 192.
[34] Y. Di, X. Wang, A. Thomas, M. Antonietti, *ChemCatChem* **2010**, *2*, 834.
[35] K. Guillois, L. Burel, A. Tuel, V. Caps, *Appl. Catal. A* **2012**, *1*, 415.
[36] M. Khan, H. Farah, N. Iqbal, T. Noor, M. Z. Bin Amjad, S. S. E. Bukhari, *RCS Adv.* **2021**, *11*, 37575.
[37] W.-J. Ong, L.-L. Tan, Y.-H. Ng, S.-T. Yong, S.-P. Chai, *Chem. Rev.* **2016**, *116*, 7159.
[38] P. Jimenez-Calvo, M. N. Ghazzal, V. Caps, C. Colbeau-Justin, V. Keller, *Nano Energy*, **2020**, *75*, 104888.
[39] Y. Jiang, H. Zhang, Q. Chen, Z. Sun, L. Zeng, *Appl. Surf. Sci.* **2022**, *9*, 100238.
[40] P. Jiménez-Calvo, L. Michel, V. Keller, V. Caps, *ACS Appl. Mater. Int.* **2021**, *13*, 61015.
[41] S. C. Warren, E. Thimsen, *Energy Environ. Sci.* **2012**, *5*, 5133.
[42] O. A. Tahiri Alaoui, C. Herissan, M. E. Le Quoc, M. Zekri, S. Sorgues, H. Remita, C. Colbeau-Justin, *J. Photochem. Photobiol. A* **2012**, *242*, 34.
[43] Y. Zhou, L. Zhang, W. Huang, Q. Kong, X. Fan, M. Wang, J. Shi, *Carbon* **2016**, *99*, 111.
[44] J. Fu, K. Liu, K. Jiang, H. Li, P. An, W. Li, N. Zhang, H. Li, X. Xu, H. Zhou, D. Tang, X. Wang, X. Qiu, M. Liu, *Adv. Sci.* **2019**, 1900796.
[45] F. Vigneron, A. Piquet, W. Baaziz, P. Ronot, A. Boos, I. Janowska, C. Pham-Huu, C. Petit, V. Caps, *Catal. Today* **2014**, *235*, 90.
[46] P. Jimenez-Calvo, C. Marchal, T. Cottineau, V. Caps, V. Keller, *J. Mater. Chem. A* **2019**, *7*, 14849.
[47] C. Colbeau-Justin, M. Kunst, D. Huguenin, *J. Mater. Sci.* **2003**, *38*, 24.
[48] S. Bardey, A. Bonduelle-Skrzypczak, A. Fécant, C. Zhznpznq, C. Colbeau-Justin, V. Caps, V. Keller, *Faraday Discuss.* **2019**, *214* 417.
[49] Y. Zhang, D. Yao, B. Xia, M. Jaroniec, J. Ran, S.-Z. Qiao, *ACS Energy Lett.* **2022**, *7*, 1611.